Chaotic Analysis of the Reversible Pump Turbine Exhaust Process in Pump Mode Based on a Data-driven Method

F. Zhang[1,2], M. Fang[1,2], R. Tao[1,2], D. Zhu[3], W. Liu[4], F. Lin[4] and R. Xiao[1,2, †]

[1] *College of Water Resources and Civil Engineering, China Agricultural University, Beijing, 100083, China*
[2] *Beijing Engineering Research Center of Safety and Energy Saving Technology for Water Supply Network System, China Agricultural University, Beijing 100083, China*
[3] *College of Engineering, China Agricultural University, Beijing 100083, China*
[4] *Dongfang Electric Machinery Co. Ltd., Deyang, Sichuan, 618000, China*

†*Corresponding Author Email: xrf@cau.edu.cn*

ABSTRACT

Due to the important strategic position of Pumped Storage Power Plants (PSPP) in global energy upgrading, conducting in-depth research on the various operating conditions of pump turbine units is important for their safe and stable operation. This study sought to clarify the gas–liquid phase motion and the nonlinear chaotic characteristics of the process of exhaust and pressurization in pump mode; with the simplified objective model proposed here, a visualization of the process is achieved using data-driven methods, and the nonlinear characteristics of gas–liquid phase motion during the process are theoretically demonstrated. A method that combines data-driven and chaotic analysis is proposed to qualitatively and quantitatively analyze the force and torque time-series signals of the runner under different exhaust rates. The results indicate that the chaotic characteristics of the force signals and torque signals of the runner are not in a single linear relationship with the exhaust rates. Therefore, this research also provides guidance on exhaust rates with the aim of informing actual engineering practice, the purpose of which is to reduce the vibration amplitude caused by repetitive torque and improve the stability of the unit operations.

1. INTRODUCTION

Energy upgrading is an essential process for social development (Ji & Zhang, 2019). Energy upgrading in the 21st century involves a comprehensive upgrade from 'non-renewable energy' to 'renewable green energy' (Hanjra & Qureshi, 2010). The Paris Agreement, passed in 2015, marks the beginning of the transition to a low-carbon world (Nishioka, 2023). However, energy upgrading also faces multifaceted challenges, with combustion and complex new energy technologies experiencing multiple issues, such as technological research and development (Ardizzon et al., 2014).

Among the numerous extant renewable energy sources, such as energy from wind, solar system and hydropower, hydropower has been widely used due to its high energy conversion efficiency and outstanding peak shaving and frequency regulation capabilities in the power grid (Zhao et al., 2020). Pumped Storage Power Plants (PSPP) are the main force in the utilization of hydropower and are also recognized as reliable peak shaving and frequency regulation power sources worldwide (Staub et al., 2018). Due to the outstanding regulation ability of PSPP for the power system during operations, they can both cut peaks and fill valleys, adapt well to changes in power system loads, and simultaneously store and convert electricity (Wanfeng et al., 2021). They have been widely used and play an important role in the energy transformation (Al-Obaidi, 2023). The reversible pump turbine is set as the core of energy conversion in PSPP, and, as a working principle, it mainly operates in various modes of forward and reverse rotation of the runner (Murakami & Kanemoto, 2013). The main working condition of a reversible pump turbine is to enter the mode with generating power when the power grid load is high: that is, the turbine mode (Al-Obaidi, 2024a). The fluid flows from the upstream reservoir downstream, and the impact wheel rotates to drive the generator to generate electricity, sharing the power pressure of grid (Al-Obaidi, et al. 2022a). When the power grid load is low, it enters the energy storage mode (Al-Obaidi, 2024b). The unit pumps fluid, consuming excess electricity in the power grid

Nomenclature

GGI	General Grid Interface	D_2	outlet diameter of runner
PSPP	Pumped Storage Power Plant	e	the value of time delay
∇	Nabla operator	f_v	liquid volume fraction
∇^2	Laplacian operator	F_1	blending function
$\mathbf{u}$	velocity vector	F_r	radial force of runner
$\mathbf{f}$	stress vector	F_Z	axial force of runner
α_0	studied guide vane opening	H_r	rated hydraulic head
θ	position angle of data points in phase space	l	torque of runner
β	constant of the turbulence model	ly-max	maximum Lyapunov exponent
β^*	constant of the turbulence model	L	liquid level
μ	dynamic viscosity coefficient of fluid	m	embedding dimension
μ_t	turbulent eddy viscosity	N	number of data set
ρ	density of the fluid medium	N_s	number of disjoint subsequences
σ_k	constant of the turbulence model	p	static pressure
σ_ω	constant of the turbulence model	P_k	production term of turbulent kinetic energy
τ	time delay	r	relative mesh spacing
τ_d	optimal time delay	r'	radius from data point to origin in phase space
τ_w	delay time window	S	detection statistic
B	guide vane height	t	value of time delay
C	correlation integral	u_x	velocity vector in x direction
C_s	correlation integral of time series when the detection statistic $s=1$	u_y	velocity vector in y direction
C_{ms}	correlation integral of time series when the detection statistic $s=1$ and the embedding dimension $m=1$	u_z	velocity vector in z direction
d_{ij}	distance of two points in the phase space	v	exhaust rate
D_1	inlet diameter of runner	Z_r	number of runner blades

while preparing for the next power generation mode (Vick & Neal, 2012; Cavazzini et al., 2018). In addition to the conversion process of the two main working conditions, its operation also undergoes many transient processes (Al-Obaidi et al. 2022b). Li et al. (2018) conducted a numerical simulation of the closing process of the guide vanes under pump operating conditions and found that the instability of the process is caused by severe fluctuations and eddies in the guide vane and stay vane. However, no further analysis was conducted on the exhaust process after the guide vanes were closed. Kan et al. (2021) compared the prediction accuracy of the volume of fluids (VOF) and rigid lid hypothesis (RLH) methods when predicting the transient characteristics of pump outage processes; they proposed a new prediction model for transient process research. Zuo et al. (2016) summarized the instability problems of various transient processes caused by the 'S' characteristics of pump turbines in turbine mode; they provided measures to improve the instability of transient processes. Al-Obaidi et al. & Alhamid (2023) studied the mechanism of hydrodynamic instability of hydraulic machinery blade angles using a combination of numerical simulations and experiments, and the research results indicated that changes in the runner blade angle influenced the machine's flow and pressure field characteristics. The method of this study is useful and can be used when researching transient processes in pump turbines. However, there was almost no discussion of the instability of the exhaust process when starting at pump mode. The importance of the reversible pump turbine to energy upgrading makes every pump turbine process worth

studying. In many transient processes, before the pump mode is instigated, it usually undergoes a process of exhaust and pressurization in order to exhaust the gas and increase the pressure inside the unit (Jain & Patel, 2014). During this process, the guide vane is totally closed, the rotation speed of runner is relatively high. The amount of gas residue in this process, as well as the exhaust rate, directly affects the stability of the pump start up and the performance in pump mode (Al-Obaidi, 2018). In other words, if the exhaust rate of the process is too slow, the fluid stays in runner chamber for too long and collides with the unit at high speed, causing the repetitive torque of the runner and leading to vibration problems in the unit. In addition, if the exhaust rate is too low, it will also prolong the entire transition process and reduce the economic benefits of the power station. If the exhaust rate is too fast, it will cause the liquid surface to enter the runner too early, causing repetitive torque inside the runner and the vibration of the unit. Nevertheless, there is little detailed discussion of the exhaust and pressurization in the existing research.

The process of exhaust and pressurization is complex, which ultimately involves the problem of gas–liquid two phases flow (Zhang et al., 2023). The root cause of the system's complexity is nonlinearity (Fengxia et al., 2019). A two-phase flow is a representative nonlinear dissipative dynamic system, the extraction of the flow process's characteristic quantities and dynamics is highly significant for flow guidance and engineering applications (Liu et al., 2019). Nonlinear information processing technology also provides a new basis for gas–liquid phase flow signal analysis (Al-Obaidi, 2019). Attractor

morphology is a method proposed in recent years for analyzing the nonlinear characteristics of time-series signals (Zhang et al., 2021). This method analyzes statistical feature quantities based on the geometric morphology of attractors in phase space of nonlinear time-series signals to analyze the nonlinear information contained within them. Chaotic characteristics are attributes of nonlinear systems, which means that all nonlinear systems or signals have chaotic characteristics (Guo & Xu, 2022). Chaos is a possible stationary state of nonlinear dynamic systems, but the chaotic time series is neither monotonically changing nor periodic; instead, it appears to have a random inverse periodic motion (Fahlbeck et al., 2021). Chaos is a common phenomenon in nature and human society, comprising a complex nonlinear and non-equilibrium dynamic process. Chaos was first proposed by Yoke and Tianyan Li in their paper 'Period Three Implies Chaos', published in 1975, which revealed the unity of order and disorder in objective things, as well as the unity of certainty and randomness (Zhou et al., 2018). For practical dynamic systems, research on time series is conducted in the phase space, and the first step of chaotic analysis is to reconstruct phase space as well.

The principal methods used to reconstruct phase space for time series include the derivative reconstruction method and the coordinate delay reconstruction method which are proposed by Packard et al. (Breedon & Packard, 1992). However, there is no known prior information before analyzing entire time-series signal; in addition, from the perspective of numerical calculations, the numerical differentiation in the derivative reconstruction method is a calculation process that is highly sensitive to errors. Therefore, in order to make sure the accuracy of the phase space reconstruction without error accumulation, coordinate delay reconstruction method is usually used to analyze the phase space reconstruction problem in chaotic signals (Zheng et al., 2020). When using the coordinate delay reconstruction method to reconstruct phase space, the most important thing is to determine the embedding dimension m and time delay τ (Matilla-García et al., 2021). The 'Takens' theorem indicates that, for ideal one-dimensional time-series signals, the embedding dimension and time delay can take any value (Sauer et al., 1991). However, in practical applications, time-series signals are sequences with finite length that contain noise, the embedding dimension and time delay cannot take any value. If they did, the quality of the reconstructed phase space will be seriously affected (Kim et al., 1999). Based on the phase space that is reconstructed, qualitative analysis of chaotic correlations in time-series signals is achieved using phase diagrams. In the process of nonlinear science and the development of chaotic systems, quantitative analysis methods are needed to quantitatively analyze the dynamic characteristics of time-series signals (Casdagli et al., 1991). Based on the theory of chaotic dynamics, scholars have proposed chaotic characteristic parameters, such as attractors, Kolmogolov entropy, and the maximum Lyapunov exponent, to quantitatively describe the dynamic characteristics of the system (Bandt & Pompe, 2002). The Lyapunov exponent analysis method has been widely used in dynamic analysis

research due to its advantages of low computational complexity, simple operations, and reliable results (Mezi, 2005). Based on the definition of chaos, it can be seen that chaotic motion is extremely sensitive to the initial value conditions. Over time, trajectories that are close to each other in the phase space either converge rapidly at exponential speeds or diverge slower than exponential speeds. The Lyapunov exponent is a characteristic quantity that quantitatively characterizes the convergence or divergence of such trajectories (Rajendra Acharya et al., 2006). This feature quantity reflects the sensitivity of system dynamics behavior to initial values over time. If the calculated value of the system is regular, it indicates that the system has chaotic characteristics, while a negative value indicates that the system has randomness or periodicity (Abarbanel et al., 1993). The larger the exponent, the stronger the nonlinearity of the system and the more sensitive it is to the initial value.

Due to the crucial position of the reversible pump turbine in PSPP, the nonlinear behavior observed during its transient operation has attracted a good deal of attention. Determining its chaotic characteristics for time-series signal diagnosis during the exhaust process is highly significant for the safety and stability of operation of pump turbines. This research focused on the process of exhaust and pressurization in starting up process of pump mode which have received less attention in existing research for its complexity. The visualization of the gas–liquid motion of the objective process is achieved by utilizing the volume fraction contours of the liquid phase via a simulation. In addition, the time-series signals of force (including axial and radial force) and torque of runner are also monitored; chaotic dynamics analysis is performed on these time-series signals under four different exhaust rates. By combining phase diagrams and maximum Lyapunov exponents, the chaotic characteristics of various time-series signals under different exhaust rates were qualitatively and quantitatively analyzed, innovatively revealed the chaotic characteristics of the force and torque signals of the runner at different exhaust speeds. This provides a reference for the stability of the exhaust process in engineering and lays a theoretical foundation for eliminating vibrations from the unit and allowing it to pass smoothly through the transient process.

2. RESEARCH OBJECTIVE

2.1 Geometric Model

Figure 1 shows whole fluid domain of the objective pump turbine in this research. The *X-Y-Z* Cartesian coordinate was established as shown in Fig. 1 (a). When the unit operates in pump mode, fluid flows along $+Y$ direction from the draft tube to the volute. In turbine mode, the fluid flows in the opposite direction. The meridional flow channel of the runner is shown in Fig. 1 (b). Table 1 shows the main parameters. During the operation process, there are frequent changes in the operating conditions. In addition to the power generation condition (turbine condition) and the energy storage condition (pump condition),
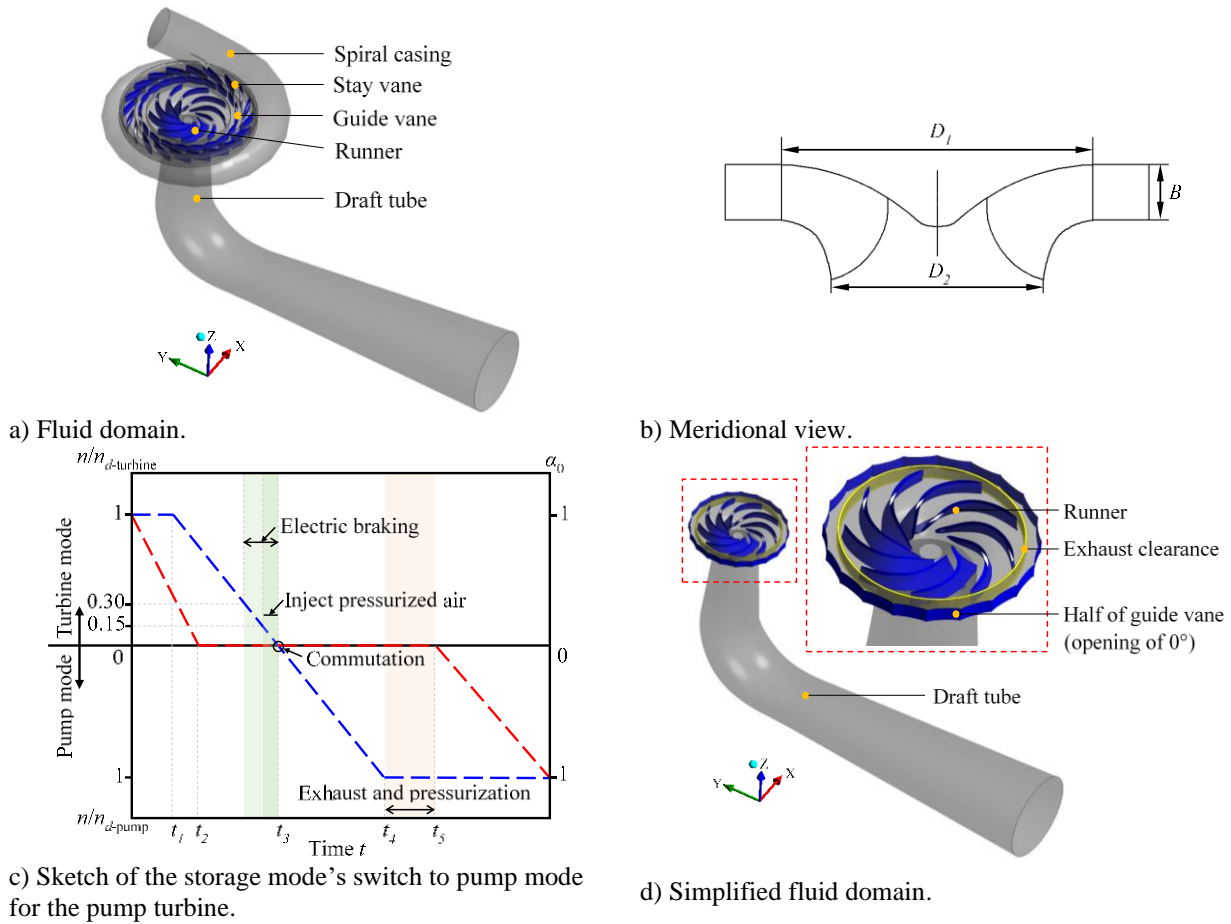
a) Fluid domain.

b) Meridional view.

c) Sketch of the storage mode's switch to pump mode for the pump turbine.

d) Simplified fluid domain.

Fig. 1 Research sketch map of the objective model

Table 1 Basic geometric parameters

Parameter	Symbol	Value	Unit
Rated hydraulic head	H_r	14.93	[m]
Inlet diameter of runner	D_1	470	[mm]
Outlet diameter of runner	D_2	252	[mm]
Guide vane height	B	43	[mm]
Number of runner blades	Z_r	9	[-]
Studied guide vane opening	α_0	0	[°]

there are also many operating conditions during the transition process.

As shown in Fig. 1 (c), when the turbine mode ends and the pump mode starts, the motor is disconnected, the unit is unloaded, and the rotation of the runner gradually slows down. The ball valve and the guide vane are shut simultaneously. After guide vane is totally closed, the slowing of the rotational speed of runner still relies impact on fluid flow inside the runner. When rotation speed drops to 15% of the rated speed, the pressure in the runner channel rises until the runner stops rotating. The liquid surface is now in draft tube. At this time, the chamber of runner is empty, the guide vane keeps totally closed, while the rotation speed is zero. The unit is connected to the power grid and started, later, the rotation speed reaches to rated speed in the rotation direction of the pump mode. At this point, the unit can be subjected to the operation of exhausting and pressurization, that is, opening the exhaust

clearance to keep the pressure inside the unit balance with the outside atmosphere, and the surface of liquid stop rising until the gas exhausted totally. Subsequently, opening the guide vane and main valves to pump fluid, completing the rapid transition from the power generation mode to the energy storage mode.

This study focuses on the characteristics of the force and torque time-series signals under different exhaust rates during the process of exhaust and pressurization in starting up process of pump mode. Because the liquid level is pressed inside the draft tube during this process, guide vane is fully shut, while runner rotates at rated speed. Therefore, simplifying whole guide vane as a wall is feasible, the simplified model fluid domain is shown in Fig. 1 (d). With this model, this study defines the exhaust rate v =0.083m/s. We conduct a detailed analysis of the exhaust pressure process at four rates: $0.5v$, v, $1.5v$, and $2v$.

2.2 Discussion of Nonlinear Problems

The exhaust and pressurization problem encountered during the start-up process ultimately boils down to the problem of the gas–liquid phase flow with the gas and the liquid. The gas–liquid two phases flow is a typical dissipative and nonlinear system, and its flow behavior has characteristics such as diversity, instability, nonlinearity, and complexity. The nonlinearity and complexity of gas–liquid two phases flow are often inherent in its fluctuation signals. The complexity of gas–

liquid flow patterns reflects the essential characteristics of nonlinear and unstable gas–liquid flow systems.

The following equation is the general form of the incompressible Navier–Stokes equation with passive terms (Gallavotti, 1996):

$$\rho\frac{\partial \mathbf{u}}{\partial t} + \rho(\mathbf{u}\cdot\nabla)\mathbf{u} = -\nabla p + \nabla\cdot(\mu\nabla\mathbf{u}) + \mathbf{f} \qquad (1)$$

where ρ represents the density, $\mathbf{u}$ represents the velocity vector, p represents the pressure, and $\mathbf{f}$ represents the stress vector.

When simulating gas–liquid phase flow processes based on numerical simulation methods, the Navier–Stokes equation is closed using a turbulence model, and the monitoring value results of each fluid particle in the flow field are solved using the deferential method. In the process of simulating and monitoring time-series signals, the nonlinear convection term in the Navier–Stokes equation is usually locally linearized, but it still does not affect the nonlinear characteristics of the CFX calculation results. The nonlinear term is also a reflection of turbulence in mathematics. In addition, the second term on the left side of the Navier–Stokes equation refers to the partial derivative of $\mathbf{u}$, which constitutes a nonlinear problem of the product of an unknown quantity and an unknown quantity. This further indicates that, when the problem studied using CFX is a nonlinear problem, the computational results of CFX have nonlinear characteristics.

3. CFD SETUP

3.1 Solver Setup

For the process of exhaust and pressurization, while the runner rotates at the rated speed, the gas–liquid phase motion inside the unit is complex and chaotic. Based on the computational fluid mechanics theory and numerical simulation methods, not only can the gas–liquid phase changes of the process be effectively simulated, visualization research can also be achieved, and the various time-varying signal changes of the process can also be monitored. With the combination of ANSYS CFX solver with the theory of fluid dynamics, this research conducts simulation results of the simplified model. For the simplified fluid domain, the inlet of the entire fluid domain is the inlet of the draft tube, and the outlet of the entire fluid domain is exhaust clearance outlet. The interface of opening pressure and direction is set as the inlet boundary, and the velocity boundary is set at the outlet. For the gas–liquid interface, a segmented function is used, and all walls are set as the no-slip type. For the interface between various components for data transmission, the dynamic–static interface is set between the runner and the components connected to it.

Throughout the numerical simulation, a combination of steady and unsteady calculations was used. In the steady state calculations, the iteration step is 1000. This study uses steady state calculations to confirm the initial level of liquid surface where there is no entrainment occurs with the highest liquid level. For the unsteady state

calculations, the time interval between each step is 0.005 seconds, and the total calculation time is 26 seconds when the speed is v. The iterations for each time step in the unsteady calculations is 5.

Throughout the simulation, the continuity equation and the momentum equation are shown as follows (Choi & Yoon, 2009), the iterative convergence index of which is 10^{-6}:

$$\frac{\partial \rho}{\partial t} + \frac{\partial(\rho u_x)}{\partial x} + \frac{\partial(\rho u_y)}{\partial y} + \frac{\partial(\rho u_z)}{\partial z} = 0 \qquad (2)$$

where ρ represents density; t represents the time; and u_x, u_y, and u_z represent the velocity vector in different directions respectively.

$$\frac{\partial(\rho\mathbf{u})}{\partial t} + (\rho\mathbf{u}\cdot\nabla)\mathbf{u} = -\nabla p + \mu\nabla^2\mathbf{u} + \rho\mathbf{f} \qquad (3)$$

where μ represents the dynamic viscosity coefficient, $\mathbf{u}$ represents the velocity vector, ∇ represents the Nabla operator, ∇^2 represents the Laplacian operator, and $\mathbf{f}$ represents the stress vector.

3.2 Turbulence Model

In numerical simulation process, a turbulence model is often used to close the Navier–Stokes equation. By comparing k-ε and k-ω series turbulence model, SST k-ω model takes the transfer of turbulent shear stress into account in detail and has good convergence in calculating two-phase flow problems, and it has high prediction accuracy in multi-phases flow. Therefore, the final prediction turbulence model for this study is SST k-ω model (Menter et al., 2003).

The equation of turbulent kinetic energy and the transport equation of dissipation rate are shown in the following (Rezaeiha et al., 2019):

$$\frac{\partial(\rho k)}{\partial t} + \frac{\partial(\rho k u_i)}{\partial x_i} =$$
$$P_k - \beta^*\rho\omega k + \frac{\partial}{\partial x_i}\left((\mu + \sigma_k\mu_t)\frac{\partial k}{\partial x_i}\right) \qquad (4)$$

$$\frac{\partial(\rho\omega)}{\partial t} + \frac{\partial(\rho\omega u_i)}{\partial x_i} =$$
$$\alpha\rho S^2 - \beta\rho\omega^2 + \frac{\partial}{\partial x_i}\left((\mu + \sigma_\omega\mu_t)\frac{\partial\omega}{\partial x_j}\right) \qquad (5)$$
$$+2(1-F_1)\rho\sigma_{\omega 2}\frac{1}{\omega}\frac{\partial k}{\partial x_i}\frac{\partial\omega}{\partial x_i}$$

where P_k represents the production term, S represents the invariant measure of the strain rate, μ represents the dynamic viscosity, F_1 represents the blending function, μ_t represents turbulent eddy viscosity, and β, β^*, σ_k, and σ_ω are constants.

3.3 Mesh Schemes with Independence Check

For numerical simulation of different flow conditions, the grid is the most basic unit for data transmission, and the accuracy and rationality of the grid topology structure are highly significant for the result of numerical simulation. The mesh division method used in this study

Table 2 Grid number of each component

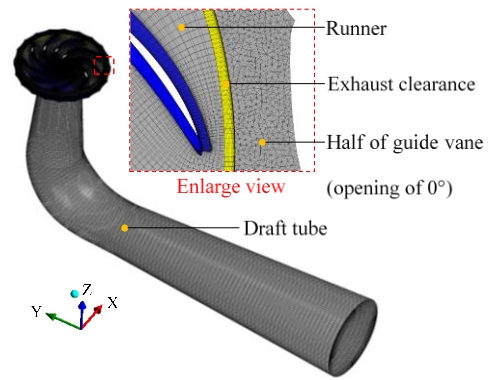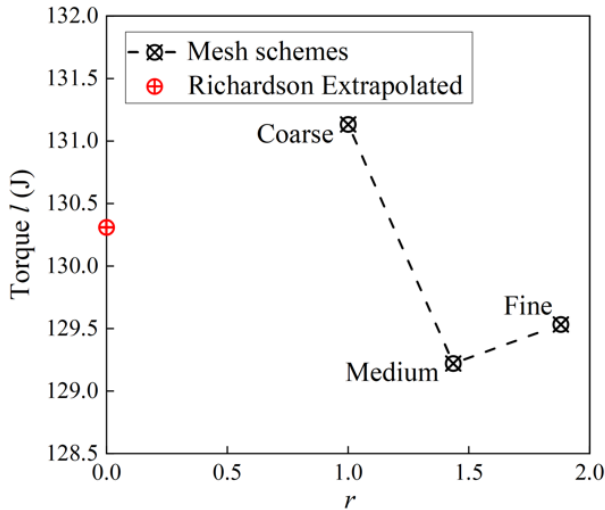| Components	Element type	Node number
Guide vane	Tetrahedral unstructured mesh	67908
Runner	Hexahedral structured mesh	420903
Clearance	Hexahedral structured mesh	29736
Draft tube	Hexahedral structured mesh	287490
Total	Mixed	806037

Fig. 2 Results of mesh independence check

combines a hexahedral structured mesh with a tetrahedral unstructured mesh. The mesh is divided using ICEM and Turbo-grid commercial software. The simplified fluid domain is discretized into grids and combined with mesh independence checks based on the Richardson extrapolation method (Celik et al., 2008). Three mesh schemes with different densities are checked for mesh independence. For three sets of mesh schemes (fine (N1), medium (N2), and coarse (N3)), the number of grids is as follows: N1=1780681, N2=806037, and N3=342081. Impeller torque is set as the key indicator for evaluating mesh independence. Calculations are conducted, and the convergence results are shown in Fig. 2, where r is the relative mesh spacing. The scale factor of N1 compared to N2 is represented by r_{12}, with a value of 1.3 and a GCI value of 2.1%. The scale factor of N2 compared to N3 is represented by r_{23}, with a value of 1.54 and a GCI value of 0.66%. According to the requirements of the mesh independence check method, a convergence index of lower than 5% is considered as convergent result. Therefore, all three sets of grids meet the mesh independence requirements. Considering the existing computing resources and ensuring the accurate transmission of data carried by the grid elements, this research selected mesh scheme N2 as the final simulated mesh. The number of elements in different components are shown in Table 2 and the final mesh scheme is shown in Fig. 3.

Fig. 3 Sketch map of final mesh scheme

4. CFD ANALYSIS

4.1 Pre-Computation

In the process of exhaust and pressurization, runner rotates and the liquid level gradually rises from the draft tube. Due to the runner rotation, as the liquid surface gradually approaches runner, the surface of the free liquid level will be shattered, leading to entrainment. Before the simulation officially begins, the initial height of the liquid level is crucial for the calculation time and the use of computing resources. If the initial level is too high, the phenomenon of entrainment of the liquid surface will occur at the beginning of the simulation process, resulting in too many gas–liquid interfaces, so that the simulation process may not converge. If the initial level is too low, the simulation process will be too long, and it will remain in the stage of the stable rising of the free surface for an extended period, wasting computational resources and time. Therefore, finding the appropriate initial position of the free liquid surface is of great significance for the computational stability and rational use of computing resources.

As shown in Fig. 4, five different initial levels were simulated at the exhaust rate of $2v$, the liquid volume fraction (f_v) contours are presented one by one. The middle plane of runner is set as the reference plane with a liquid level (L) height of zero. The initial positions of the liquid level simulated in this research are all below the reference plane: -0.1m, -0.15m, -0.2m, -0.25m, and -0.3m. At each initial liquid level, when the height is -0.2m, it is in a state where entrainment is about to occur but no liquid enters into the chamber of runner, besides, no entrainment occurs at the maximum exhaust rate, which is $2v$ here, so that no entrainment phenomenon will occur at other lower exhaust rates. Therefore, the height with a value is -0.2m is set as the initial height of liquid level.

4.2 Contour Analysis

The initial height of the liquid level discussed in section 4.1 is used as the initial position for simulating the exhaust and pressurization process at various exhaust rates. Four different exhaust rates of $0.5v$, v, $1.5v$, and $2v$ are visualized and analyzed using the contours of f_v. Due to the initial height of the liquid level remaining the same, the simulation time for the exhaust process varies depending on the exhaust rate.
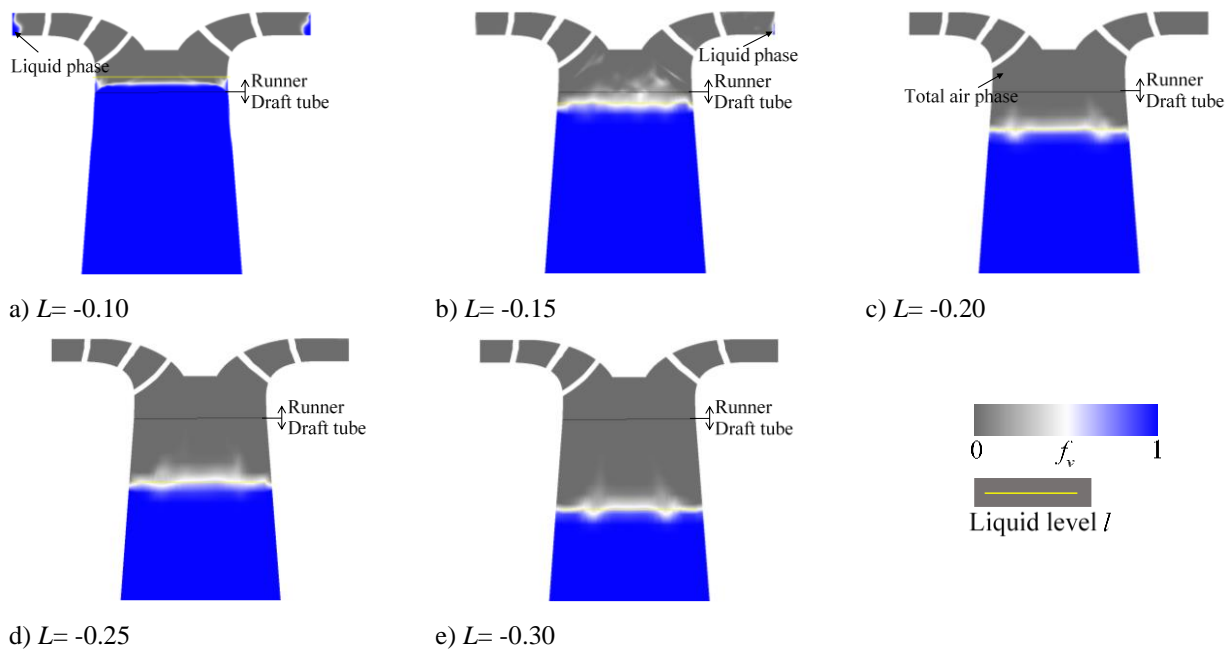
Fig. 4 Contours of f_v for different initial liquid levels

Figures 5–8 show the contours of f_v at the four different exhaust rates. At various exhaust rates, as the free liquid surface rises, the entire exhaust process can be decomposed into five main stages. The first stage is the stable rise process in the draft tube: during this part, the liquid surface steadily rises. Although the rotation speed of the runner is high, there is still no obvious breakage on the free surface of the liquid level. At this time, there are fewer interfaces for the gas–liquid phase and the motion of the gas–liquid phase is relatively stable. The second stage is confusion stage occurred in draft tube: during this stage, the free surface of the liquid is slightly broken, and the liquid level does not fully enter into the runner chamber. The rotation speed of the runner is high, which has a slight suction effect on the liquid surface. The liquid phase is thrown into the guide vane, and there is slight liquid accumulation inside guide vane. The third stage is the liquid surface entry stage in the runner: during this stage, liquid surface goes into runner, the surface is vigorously sucked, the free surface is broken, and the interfaces for the gas–liquid two phases in the runner increase, but the motion of the gas–liquid two phases is not overly chaotic. The fourth stage is the confusion stage occurred in runner: during this stage, the free surface is completely broken, the liquid phase fills the entire fluid domain, and the motion of the gas–liquid phase is highly chaotic. At this time, the vibration problem of the unit caused by repetitive torque is most likely to occur. The fifth stage is the stable development stage in the runner chamber: during this stage, the liquid surface goes into the chamber of runner totally, while exhaust process is stable. There are still interfaces for the gas–liquid phase in the draft tube, but it does not affect the entire exhaust process. When the gas is basically exhausted, the water flow inside the runner connects and reaches the closing head instantaneously. At this time, the guide vanes are closed, forming a sizeable backflow in the draft tube. This process is brief and intense. The small number of bubbles in draft tube and a small amount of the remaining gas in the runner chamber can be instantly discharged after the guide vane is opened.

For the four different rates ranging from $0.5v$ to $2v$, as the speed increases, the time proportion of the first and second stages gradually decreases. This means that, as the speed increases, the time at which the liquid goes into the runner is earlier. For the third and fourth stages, as the speed increases, the free surface undergoes severe fragmentation, but there is no significant increase for interfaces for the gas–liquid phase. For the fifth stage, there is a slight increase in the amount of residual gas in the runner chamber as the exhaust rate increases.

Figure 5 shows the contours of the f_v at different times when the exhaust rate is $0.5v$. Starting from the eighth second, the liquid surface goes into the runner, and the number of gas-liquid interfaces increase. When the exhaust process reaches 10s, due to the suction effect, a long strip-shaped cavity gradually forms and fills the entire draft tube. When the exhaust process reaches 26s, the free surface totally enters the runner, and the exhaust process stabilizes. The elongated cavity and the gas–liquid interfaces begin to decrease. When the exhaust process reaches 40s, the entire exhaust process is basically completed and the gas phase throughout the entire domain is more or less emptied.

Figure 6 shows the contours of the f_v at different times when the exhaust rate is v. Starting from the fourth second, the liquid level enters the runner, and the number of gas–liquid interfaces increases; liquid is accumulated in the guide vane. When the exhaust process reaches 6s, the surface totally goes into runner. When time reaches 12s, the surface of is severely broken and the gas–liquid phases are relatively chaotic. When the exhaust process reaches16s, the elongated cavity begins to decrease, and the exhaust process further develops until the guide
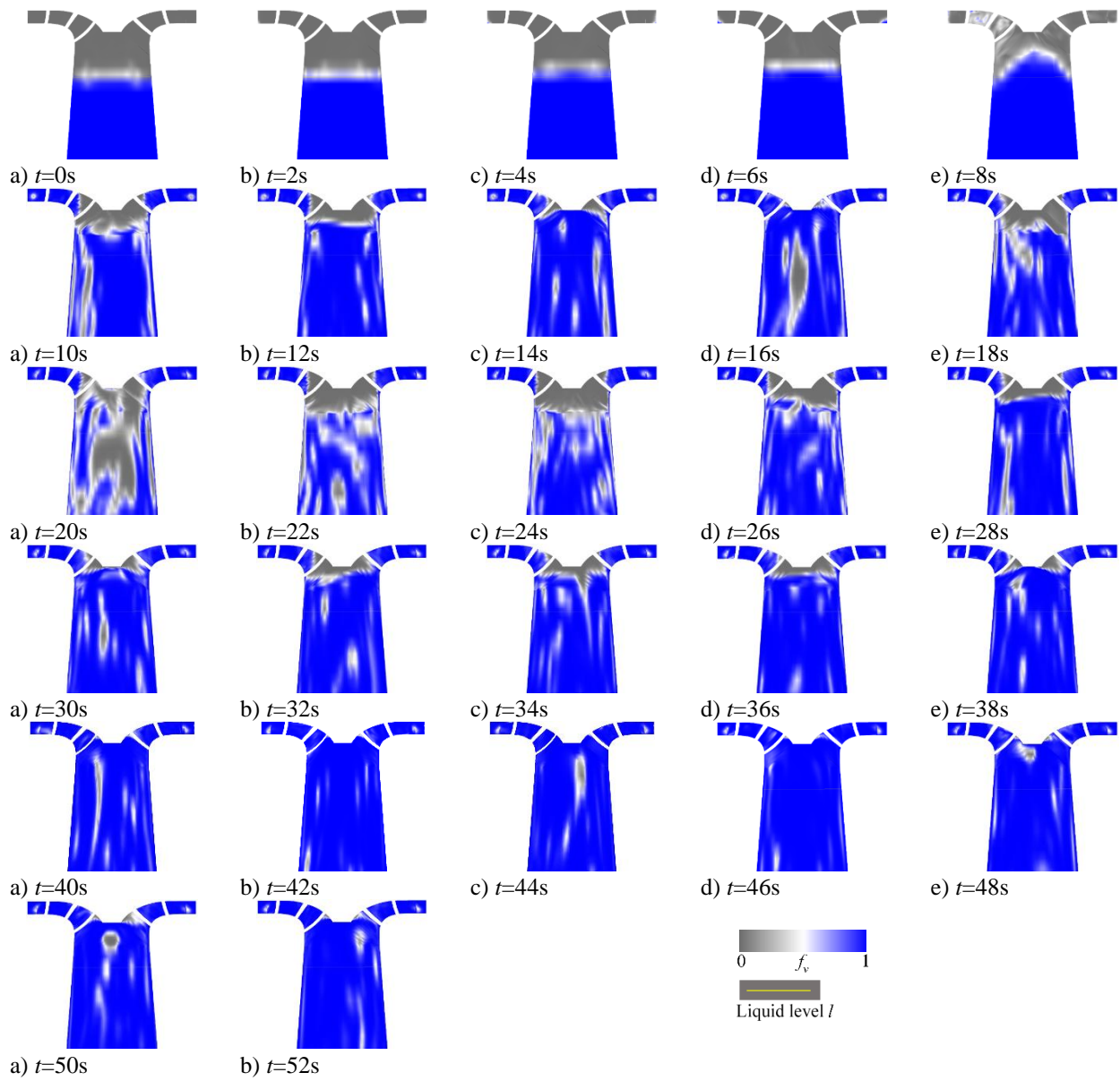
a) *t*=0s b) *t*=2s c) *t*=4s d) *t*=6s e) *t*=8s

a) *t*=10s b) *t*=12s c) *t*=14s d) *t*=16s e) *t*=18s

a) *t*=20s b) *t*=22s c) *t*=24s d) *t*=26s e) *t*=28s

a) *t*=30s b) *t*=32s c) *t*=34s d) *t*=36s e) *t*=38s

a) *t*=40s b) *t*=42s c) *t*=44s d) *t*=46s e) *t*=48s

a) *t*=50s b) *t*=52s

Fig. 5 Contours of f_v for an exhaust rate of 0.5v

(a) *t*=0s (b) *t*=2s (c) *t*=4s (d) *t*=6s (e) *t*=8s

(f) *t*=10s (g) *t*=12s (h) *t*=14s (i) *t*=16s (j) *t*=18s

(k) *t*=20s (l) *t*=22s (m) *t*=24s (n) *t*=26s
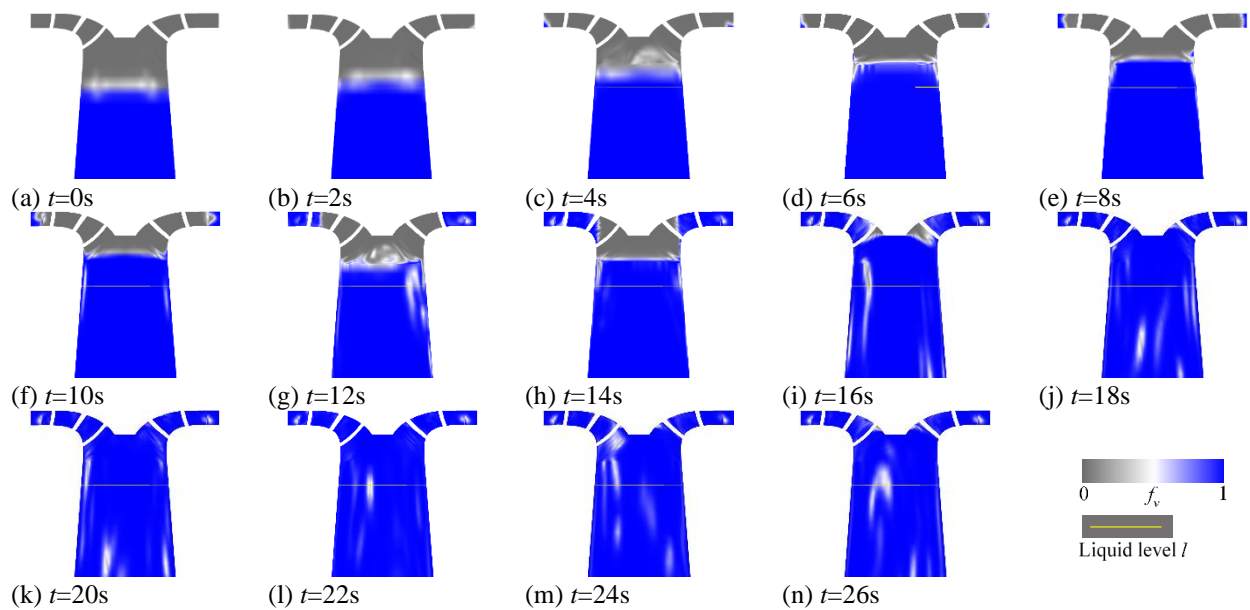
Fig. 6 Contours of f_v for an exhaust rate of v
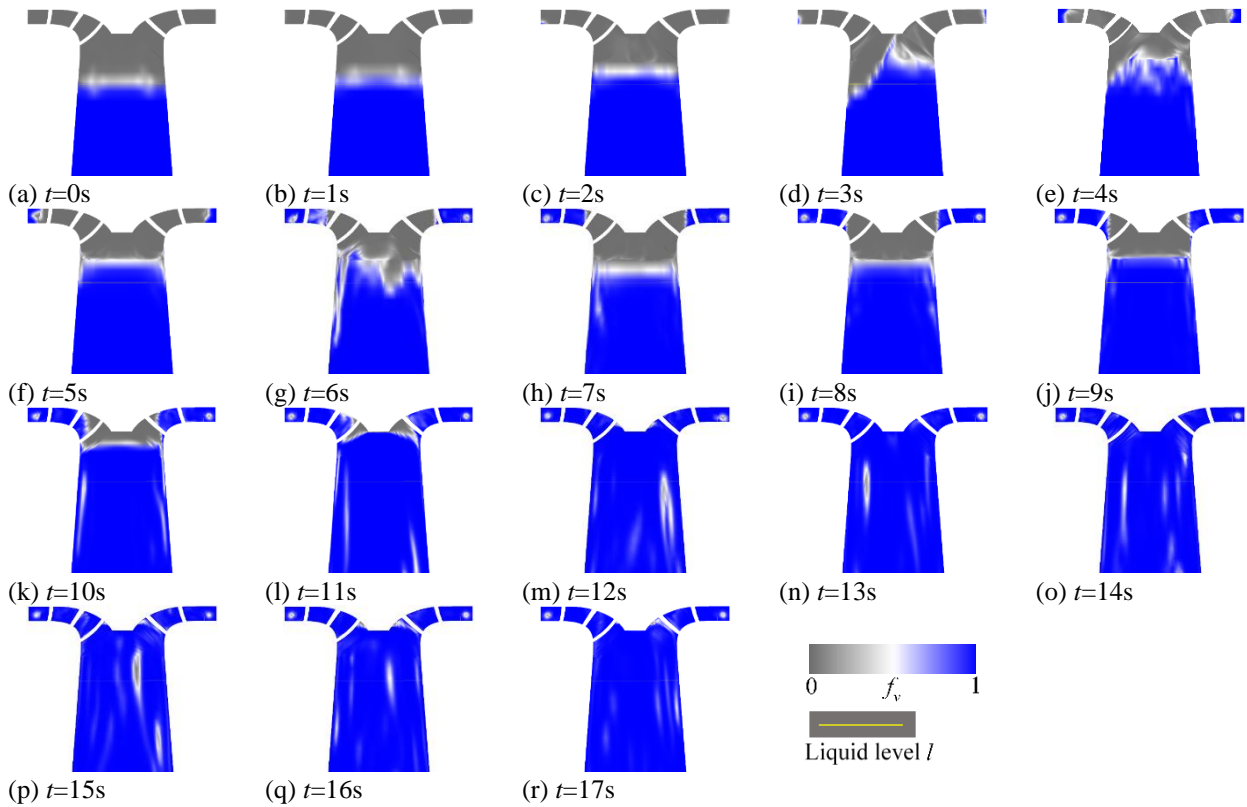
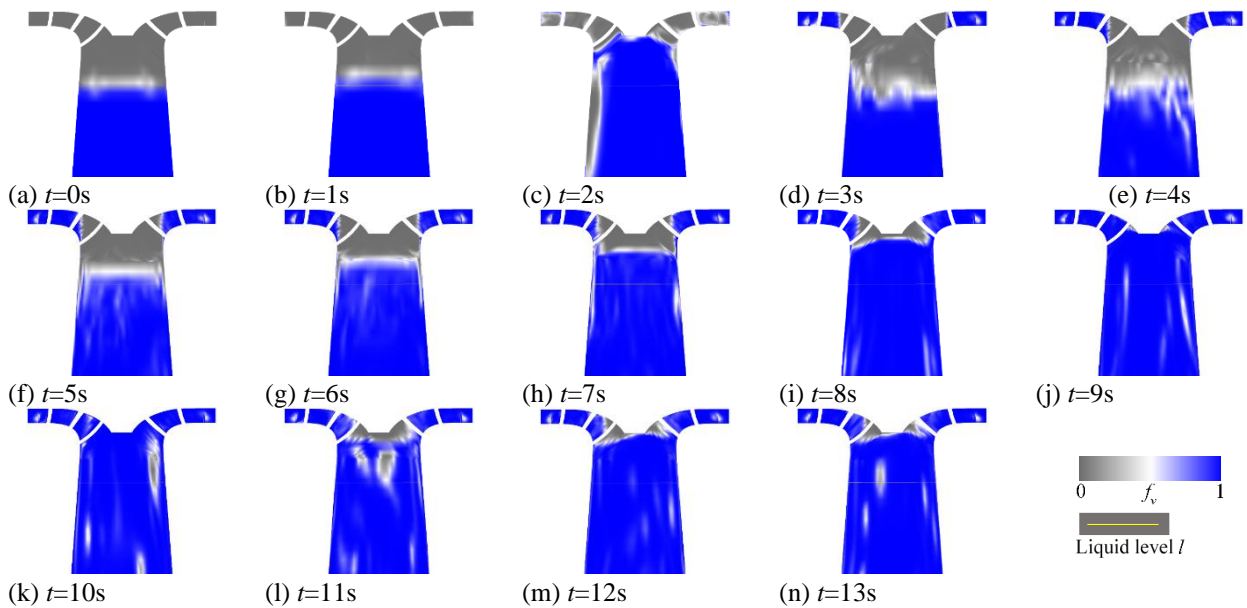**Fig. 7 Contours of f_v for an exhaust rate of 1.5v**

Fig. 8 Contours of f_v for an exhaust rate of 2v

vane is completely filled with the liquid phase. At the end of the exhaust process, the small amount of residual gas in the runner is totally eliminated after the guide vane is opened.

Figure 7 shows the contours of the f_v at different times when the exhaust rate is 1.5v. Starting from 3s, the free surface undergoes fragmentation due to the suction effect, causing chaos in the gas–liquid phase. When the exhaust process reaches 9s, the surface totally enters into runner. At 10s into the exhaust process, the elongated cavity begins to rise and the exhaust process gradually

approaches its end. When the exhaust process reaches 12s, the entire unit is basically filled with the liquid phase.

Figure 8 shows the contours of the f_v at different times when the exhaust rate is 2v. Starting from 2s, due to the entrainment of the free surface, the gas–liquid phases are chaotic, and a long strip-shaped cavity is generated in the draft tube. When the exhaust process reaches 3s, due to the centrifugal action, the guide vane is full of liquid, in draft tube, the two phases is chaotic, but the free surface does not fully enter into the runner. At 6s, the surface goes into runner totally, while exhaust process enters a stable development stage. When the exhaust process reaches 9s,
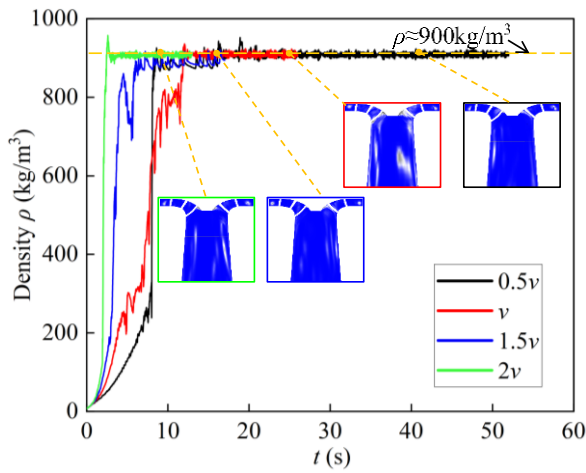
Fig. 9 Change in density inside the guide vane under various exhaust rates
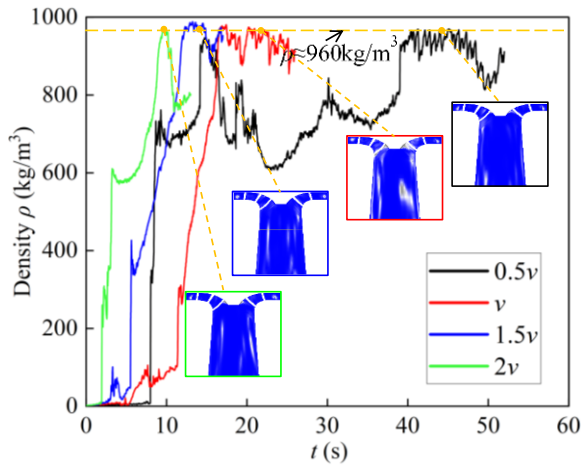

Fig. 10 Change in density inside the runner under various exhaust rates

the gas in the runner is basically exhausted, but there is still a long strip-shaped cavity containing some gas in draft tube. As the exhaust process reaches 12s, the residual gas in the runner only exists at the runner outlet. When the guide vane is opened, the gas can be quickly exhausted.

The contours of the f_v facilitated a visual analysis of the unit under different exhaust rates. In addition, this study also monitored the changes in density over time in the runner and guide vanes, combining numerical and geometric analyses to achieve a multidimensional analysis. Fig. 9 shows the variation curve of density within the guide vane over time. As the exhaust rate increases, the time to reach an almost completely liquid phase density within the guide vane is decreased, meaning that the peak of the density curve appears earlier. At various rates, when the density inside the guide vane reaches a density close to that of the full liquid, the density values inside the guide vane fluctuate around it. The contours of the f_v at that time are extracted and are consistent with the data display.

Figure 10 shows the variation curve of the density in the runner over time, similar to the density variation curve in the guide vane. The higher the exhaust rate, the sooner

the density in the runner reaches the full liquid phase density, and the earlier the peak of the density curve appears. However, the difference is that, due to the runner rotates at high speed, the motion of the gas–liquid phase inside the runner is complex. Before completely reaching the peak density of the liquid phase, other peaks occur. These peaks record the time when the liquid surface is sucked up by the runner, and the instantaneous density of the medium inside the runner chamber increases. The higher the exhaust rate, the earlier the peak appears. This is consistent with the analysis results for the contours of the f_v. The higher the exhaust rate, the earlier the free surface entrainment phenomenon occurs.

5. CHAOS ANALYSIS

Based on the nonlinear discussion of the problem addressed in section 2.2, the gas–liquid two phases flow is a typical nonlinear system with chaotic characteristics. This research aims to monitor changes of force and torque of runner over time during the process of exhaust, with the goal of obtaining three sets of time-series signals. The chaotic characteristics of the three sets of time-series signals under the four different exhaust rates studied are analyzed in detail.

5.1 Reconstructed Phase Space

The study of time-series signals is mainly conducted in the time or transformation domain. For chaotic time-series signals, whether the calculation or the prediction of chaotic invariants or models, the process is operated in the phase space. Therefore, the first step in analyzing the chaotic characteristics of time-series signals is to reconstruct phase space.

Two main types of methods are used to confirm the embedding dimension (m) and time delay (τ). The first type considers the m and τ to be independent of each other, and first calculates τ before selecting the appropriate m. The second type of method assumes that the m and τ are related; it can simultaneously calculate the τ and m. Among the numerous methods used to obtain m and τ, this study selects the representative C-C Algorithm to determine the τ and m to get reconstructed phase space.

When using the method that simultaneously determines m and τ, the time window length proposed by Kugiumtzis in 1996 is an important parameter that comprehensively considers both. That is, the determination of the τ is not independent of m but depends on the delay time window (τ_w). The relevant equation is shown as follows (Wolf et al., 1985):

$$\tau_w = (m-1)\tau \tag{6}$$

where m represents the embedding dimension and τ represents the delay time.

In 1999, C-C method was proposed by Kim et al, (1999), which advances the concept of the time window. Its main steps are as following:

The correlation integral C of the time series $y(t)$ can be defined as (Kim et al., 1999):

Table 3 Time delay and embedding dimensions

	τ	m		τ	m		τ	m		τ	m
F_r-0.5v	4	3	F_r-v	4	3	F_r-1.5v	6	2	F_r-2v	8	2
F_Z-0.5v	5	2	F_Z-v	5	2	F_Z-1.5v	8	2	F_Z-2v	5	2
l-0.5v	4	3	l-v	6	3	l-1.5v	8	3	l-2v	10	2

$$C(m,N,r',e) = \frac{2}{N(N-1)} \sum_{1 \le i \le j \le M} \theta(r'-d_{ij}) \qquad (7)$$

where N represents the number of the data set, r' represents the radius from the data point to the origin in phase space, θ represents the position angle of data points in phase space, e represents the value of the time delay, and $\tau d_{ij} = \|y_i - y_j\|_\infty$ represents the distance of two points in phase space.

The correlation integral represents a cumulative distribution function which represents the probability that the distance between any two points in the phase space is smaller than the radius r', where the distance between points is represented by the infinite norm of the vector difference. The detection statistic S_1, used to calculate the probability that the distance between two points is smaller than the radius r', is defined as (Kim et al., 1999):

$$S_1(m,N,r',e) = \\ C(m,N,r',e) - C_m(1,N,r',e) \qquad (8)$$

where C_m represents the correlation integral of the time series when $m=1$.

In the actual calculation of the above equation, it is necessary to first split the time series $\{x(n)\}$ into e disjoint subsequences, all of which have a length of $N_s = N/e$. After block averaging, the detection statistic for each subsequence S_2 is calculated as follows (Kim et al., 1999):

$$S_2(m,r',e) = \\ \frac{1}{e} \sum_{S=1} \left[C_s \left(m, \frac{N}{e}, r', e \right) - C_{m_s} \left(1, \frac{N}{e}, r', e \right) \right] \qquad (9)$$

where C_s represents the correlation integral when the detection statistic $S=1$, and C_{ms} represents the correlation integral when the detection statistic $S=1$ and $m=1$.

The two radii r' corresponding to the maximum and minimum values are selected to measure the maximum deviation of all radii, and the difference can be defined as (Kim et al., 1999):

$$\Delta S_2(m,e) = \\ \max\{S_2(m,r_j',e)\} - \min\{S_2(m,r_j',e)\} \qquad (10)$$

The local maximum time should be the zero points of $S_2(m, r', e)$ and the minimum value of $\Delta S_2(m, e)$; the optimal time delay τ_d corresponds to the first value of these local maximum values.

The detection statistic for each subsequence is simplified as (Kim et al., 1999):

$$S_2(e) = \Delta \bar{S}_2(e) + |\bar{S}_2(e)| \qquad (11)$$

Taking the global minimum of $S_2(e)$ as the time window length of the objective time series, the embedding dimension is calculated based on the time window length equation.

According to the above method, as shown in Table 3, the m and τ for the time series of the radial force (F_r), axial force (F_Z), and torque (l) at the four studied exhaust rates were determined.

The phase space of each time series is reconstructed by coordinate delay method, and principal component analysis is performed on the time series with the value of embedding dimension greater than 2 to show the phase space clearly. The value of embedding dimension greater than 2 means that analyzing the chaos characteristic for the studied time-series signals is meaningful. The first two principal components are selected for the visual analysis of the phase diagram, which is shown in Fig. 11. The values on the coordinate axis in the figure represent the measurement of the signal itself, and the degree of signal dispersion is mainly determined by the dispersion degree of the phase diagram, regardless of the size of the values. For the time-series signal formed by the radial force of the runner changing with time, as the exhaust rate increases, the dispersion degree of the reconstructed signals decreases, indicating that the chaotic degree of the radial force signal gradually weakens with the rise of the exhaust rate. For axial force time-series signal, as the exhaust rate rises, the dispersion degree of its attractor is not linearly related. At 1.5v, the dispersion degree of the axial force signal attractor is the lowest, and, at 0.5v, the dispersion degree is the highest. This indicates that, at an exhaust rate of 1.5v, the fluctuation in the axial force of the runner is relatively small. For the torque time-series signal, as the exhaust rate rises, the dispersion degree of the torque signal attractor is the lowest at 1.5v and the highest at 0.5v. This indicates that the chaos degree of the runner torque signal is the lowest at an exhaust rate of 1.5v. The phase diagram qualitatively analyzes the degree of chaos of various parameters at different exhaust rates.

5.2 Small data volume method

This research combines qualitative and quantitative methods to confirm the chaotic characteristics of each time-series signal. The phase diagram qualitatively illustrates the degree of chaos of each parameter at each exhaust rate. The Lyapunov exponent quantitatively describes the exhaust rate at which adjacent phase space trajectories diverge or converge exponentially. At least one positive Lyapunov exponent is an important indicator to make sure whether the system is in a chaotic state.

In 1985, Wolf et al. (1985) first proposed an orbit tracking method for estimating Lyapunov exponents from time series, which directly estimates Lyapunov exponents based on the long-term evolution of phase trajectories,
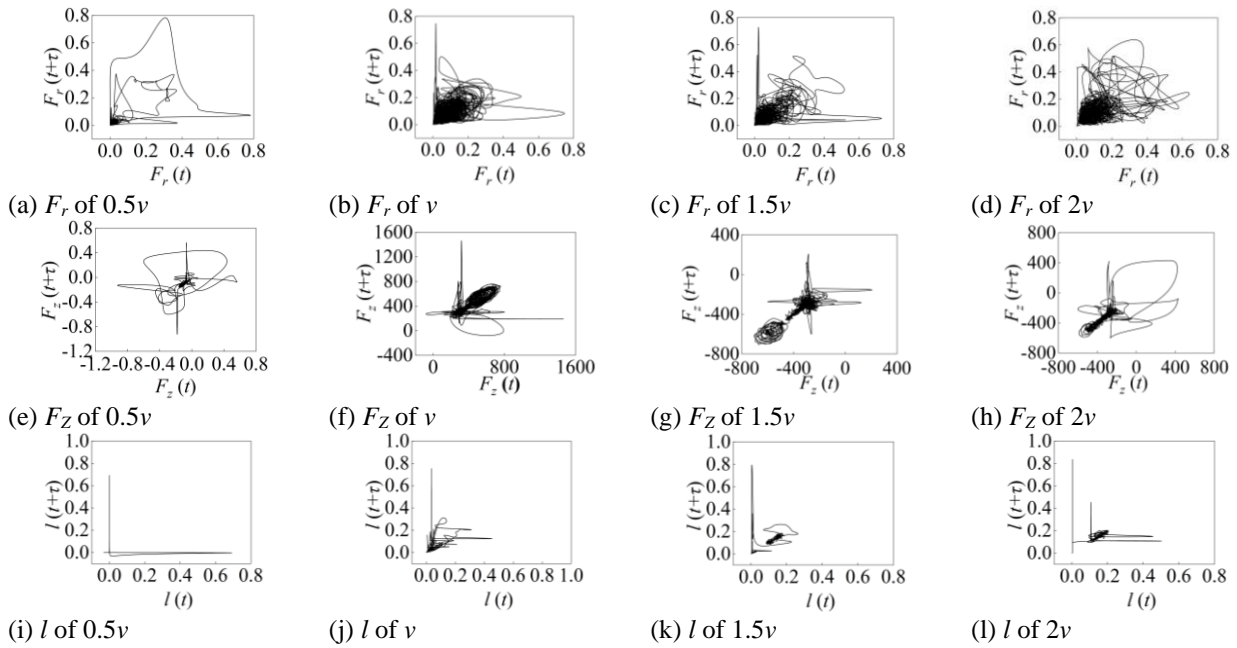
(a) F_r of 0.5v (b) F_r of v (c) F_r of 1.5v (d) F_r of 2v

(e) F_Z of 0.5v (f) F_Z of v (g) F_Z of 1.5v (h) F_Z of 2v

(i) l of 0.5v (j) l of v (k) l of 1.5v (l) l of 2v

Fig. 11 Phase diagram of timing signals under various exhaust rates

Table 4 Maximum Lyapunov exponent

	ly-max ($\times 10^{-4}$)		ly-max ($\times 10^{-4}$)		ly-max ($\times 10^{-4}$)		ly-max ($\times 10^{-4}$)
F_r-0.5v	7.04731	F_r-v	6.73272	F_r-1.5v	5.73551	F_r-2v	0.83056
F_Z-0.5v	6.71174	F_Z-v	5.53884	F_Z-1.5v	1.21198	F_Z-2v	3.63316
l-0.5v	8.80519	l-v	1.33146	l-1.5v	0.06466	l-2v	5.83122

phase planes, and phase volumes. In 1993, Rosenstein et al. (2008) improved the Wolf method with the idea of trajectory tracking and used the small data volume method to calculate the maximum Lyapunov exponent. This method fully utilizes all of the available data and achieves relatively high accuracy. The small data volume method has fast computation speeds and is easy to implement, demonstrating strong robustness to embedding dimensions, latency, and the scale of the data volume. In the process of calculating maximum Lyapunov exponent, a linear region of the $y(t)\sim t$ curve is selected and the least squares method is used to create a regression line. $y(t)$ is a general term for the time-series signal. The slope of the line is the final maximum Lyapunov exponent (ly-max). The selection of linear intervals is directly influencing the accuracy of the maximum Lyapunov exponent in characterizing chaotic signals. Therefore, before the $y(t)\sim t$ curve reaches its final saturation, an area where the $y(t)\sim t$ curve changes relatively little with t is the ideal linear region. As shown in Fig. 12, the ideal linear region selected in this research is [2,8]. Based on the selected linear region, the maximum Lyapunov exponent values of each parameter at different exhaust rates are shown in Table 4. Combined with the histogram shown in Fig. 13 where the error bars are also shown, we can clearly see the changes in the chaotic degree of the time-series signals of each parameter with the change in the exhaust rate. By quantitatively analyzing the chaotic degree of each parameter via the value of ly-max, the same conclusion can be obtained as with the qualitative analysis of the phase diagram: that is, the chaotic degree of the radial force decreases with the increase in the exhaust rate. The

degree of chaos in the axial force is at its minimum at an exhaust rate of 1.5v and at its maximum at 0.5v. The degree of chaos in the torque of the runner is at its minimum at an exhaust rate of 1.5v and at its maximum at 0.5v.

Based on the above qualitative and quantitative analysis, the chaotic characteristics of the runner force signal during the exhaust process of the entire pump turbine with different exhaust rates are not in a single linear relationship with the exhaust rate. Our findings run contrary to the conventional belief that the larger the exhaust rate, the more chaotic the signal inside the runner. In practical engineering applications, if more attention is paid to the radial force of the runner, selecting a larger exhaust rate can not only accelerate the transition process but also maintain the stable operation of the entire exhaust process. If more attention is paid to the axial force and torque of the runner, selecting an appropriate exhaust rate will not lead to the vibration problems caused by repetitive axial force and torque.

6. CONCLUSIONS

This article fills the research gap on the chaotic characteristics of force and torque signals through process of exhaust and pressurization in start-up process of pump mode. The following conclusions are drawn:

(1) This research proposed a simplified model for the process of exhaust and visualized gas–liquid phase nonlinear motion of the exhaust process based on this model. The nonlinear problem of the gas–liquid phase
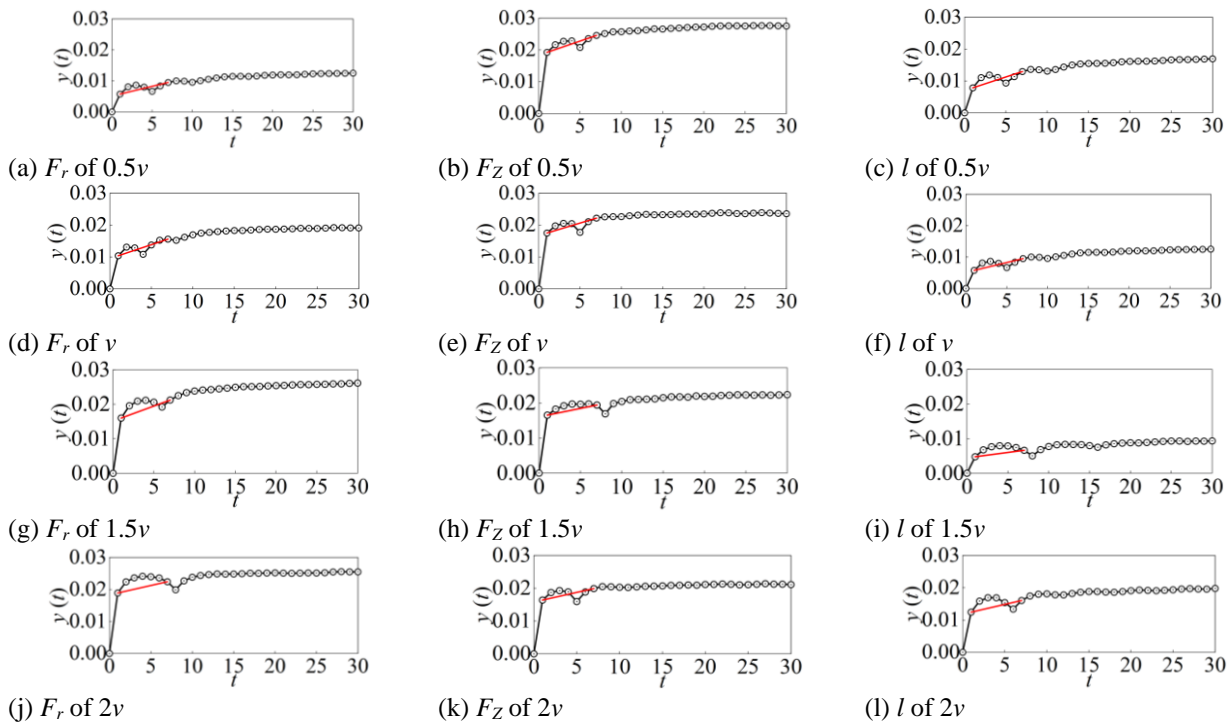
(a) F_r of 0.5v

(b) F_Z of 0.5v

(c) l of 0.5v

(d) F_r of v

(e) F_Z of v

(f) l of v

(g) F_r of 1.5v

(h) F_Z of 1.5v

(i) l of 1.5v

(j) F_r of 2v

(k) F_Z of 2v

(l) l of 2v

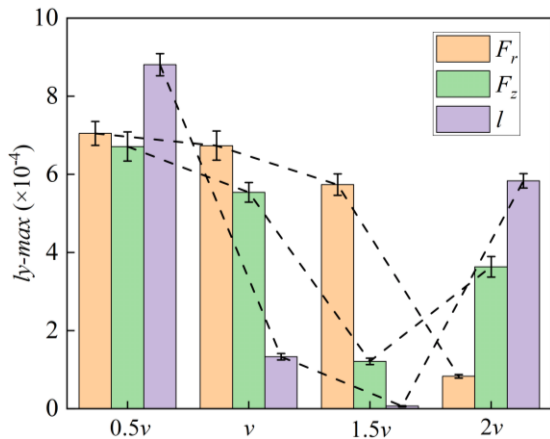**Fig. 12 Value of the Lyapunov exponent under various exhaust rates**

Fig. 13 Trend in the Lyapunov exponent under various exhaust rates

motion in this process is proposed and theoretically verified, establishing a model and a theoretical foundation for the numerical analysis of this process.

(2) This research proposed a method that combines a chaos analysis with a data-driven method to analyze transient process of pump turbine. By monitoring the time-series signals of force and torque in the exhaust process, the effective coupling relationship between the exhaust process's force and torque chaotic characteristics and vibration characteristics is obtained for different exhaust rates, and the rules are summarized to guide engineering applications. The chaotic degree of the radial force decreases with the increase in the exhaust rate. The degree of chaos in the axial force is at its minimum at an exhaust rate of 1.5v, which represents a high rate but not the highest rate, and it reaches its maximum at 0.5v, which represents a low rate. The degree of chaos in the

torque of the runner is at its minimum at an exhaust rate of 1.5v and at its maximum at 0.5v.

(3) Based on the simplified model proposed in this research and the chaos signal analysis method combining numbers and schemes, the chaotic characteristics of the force and torque signals during the exhaust process of a pump turbine are summarized. A qualitative method using a phase diagram and a quantitative method using the maximum Lyapunov exponent are combined to analyze the chaos characteristics of this process. It is found that selecting different exhaust rates in different engineering areas can effectively reduce the vibrations caused by repetitive torque and improve the operational stability of the unit.

DISCUSSION

This study analyzed the chaotic characteristics of the time-series signals of axial force, radial force, and torque through exhaust and pressurization in the start-up process of pump mode from the perspective of nonlinear dynamics. Combined with the changes of the gas–liquid two-phase flow during the process, we obtained a speed range with good chaos characteristics of force and torque for the objective unit. However, this speed range is not applicable to pump turbines that differ from the objective unit. In order to address this issue, in future work, the exhaust rate will be associated with the geometric parameters of the exhaust pipe of the pump turbine. Using optimization algorithms, the exhaust rate of the process is optimized with optimal chaotic characteristics for force and torque as the optimization objectives. The optimal exhaust rate range obtained has reference significance for pump turbine units in the same head section.

CONFLICTS OF INTERESTS

All authors declare that there is no conflict of interest in the publication of this paper.

AUTHORS CONTRIBUTION

Fangfang Zhang: Conceptualization, Methodology, Writing- Original draft preparation, Investigation. **Mingkun Fang:** Methodology, Data Curation. **Ran Tao:** Methodology, Investigation, Validation. **Di Zhu:** Investigation, Validation. **Weichao Liu:** Investigation, Validation. **Fangzhou Lin:** Investigation, Validation. **Ruofu Xiao:** Methodology, Investigation, Validation

REFERENCE

Abarbanel, H. D. I., Brown, R., Sidorowich, J. J., & Tsimring, L. S. (1993). The analysis of observed chaotic data in physical systems. *Reviews of Modern Physics, 65*(4), 1331-1392. http://doi.org/10.1103/RevModPhys.65.1331

Al-Obaidi A. R. (2024a). Evaluation and investigation of hydraulic performance characteristics in an axial pump based on CFD and acoustic analysis. *Processes, 12*(1), 129. http://doi.org/10.3390/pr12010129

Al-Obaidi, A. R. (2018). *Experimental and numerical investigations on the cavitation phenomenon in a centrifugal pump* [Doctoral thesis, University of Huddersfield]. http://eprints.hud.ac.uk/id/eprint/34513/

Al-Obaidi, A. R. (2019). Investigation of effect of pump rotational speed on performance and detection of cavitation within a centrifugal pump using vibration analysis. *Heliyon, 5*(6), e1910. http://doi.org/10.1016/j.heliyon.2019.e01910

Al-Obaidi, A. R. (2023). Experimental diagnostic of cavitation flow in the centrifugal pump under various impeller speeds based on acoustic analysis method. *Archives of Acoustics, 48*(2), 159-170. http://doi.org/10.24425/aoa.2023.145234

Al-Obaidi, A. R. (2024b). Effect of different guide vane configurations on flow field investigation and performances of an axial pump based on CFD analysis and vibration investigation. *Experimental Techniques, 48*(1), 69-88. http://doi.org/10.1007/s40799-023-00641-5

Al-Obaidi, A. R., & Alhamid, J. (2023). Investigation of the main flow characteristics mechanism and flow dynamics within an axial flow pump based on different transient load conditions. *Iranian Journal of Science and Technology, Transactions of Mechanical Engineering, 47*(4), 1397-1415.

http://doi.org/10.1007/s40997-022-00586-x

Al-Obaidi, A. R., Khalaf, H. A., & Alhamid, J. (2022a). *Investigation on the characteristics of internal flow within three-dimensional axial pump based on different flow conditions.* Proceedings of the 4th International Conference on Science Education in The Industrial Revolution 4.0. ICONSEIR 2022. http://dx.doi.org/10.4108/eai.24-11-2022.2332720

Al-Obaidi, A. R., Khalaf, H. A., & Alhamid, J. (2022b). *Investigation of the influence of varying operation configurations on flow behaviors characteristics and hydraulic axial-flow pump performance*. Proceedings of the 4th International Conference on Science Education in The Industrial Revolution 4.0. ICONSEIR 2022. http://dx.doi.org/10.4108/eai.24-11-2022.2332719

Ardizzon, G., Cavazzini, G., & Pavesi, G. (2014). A New generation of small hydro and pumped-hydro power plants: advances and future challenges. *Renewable and Sustainable Energy Reviews, 31*, 746-761. http://doi.org/10.1016/j.rser.2013.12.043

Bandt, C., & Pompe, B. (2002). Permutation entropy: a natural complexity measure for time series. *Physical Review Letters, 88*(17), 174102. http://doi.org/10.1103/PhysRevLett.88.174102

Breedon, J., & packard, N. (1992). Nonlinear-analysis of data sampled nonuniformly in time. *Physica D-Nonlinear Phenomena, 58*(1-4), 273-283. http://doi.org/10.1016/0167-2789(92)90115-4

Casdagli, M., Eubank, S., Farmer, J. D., & Gibson, J. (1991). *A theory of state space reconstruction in the presence of noise*. Springer US.

Cavazzini, G., Houdeline, J., Pavesi, G., Teller, O., & Ardizzon, G. (2018). Unstable behaviour of pump-turbines and its effects on power regulation capacity of pumped-hydro energy storage plants. *Renewable and Sustainable Energy Reviews, 94*, 399-409. http://doi.org/10.1016/j.rser.2018.06.018

Celik, I. B., Ghia, U., Roache, P. J., & Freitas, C. J. (2008). Procedure for estimation and reporting of uncertainty due to discretization in CFD applications. *Journal of Fluids Engineering-Transactions of the ASME, 130*(7). http://doi.org/10.1115/1.2960953

Choi, J., & Yoon, S. B. (2009). Numerical simulations using momentum source wave-maker applied to RANS equation model. *Coastal Engineering, 56*(10), 1043-1060. http://doi.org/10.1016/j.coastaleng.2009.06.009

Fahlbeck, J., Nilsson, H., & Salehi, S. (2021). Flow characteristics of preliminary shutdown and startup sequences for a model counter-rotating pump-turbine. *Energies, 14*(12), 3593. http://doi.org/10.3390/en14123593

Fengxia, S., Junhu, Y., Senchun, M., & Xiaohui, W. (2019). Investigation on the power loss and radial force characteristics of pump as turbine under gas–liquid two-phase condition. *Advances in Mechanical*

Engineering, 11(4), 2072153461. http://doi.org/10.1177/168781401984 3732

Gallavotti, G. (1996). Equivalence of dynamical ensembles and navier-stokes equations. *Physics Letters A, 223*(1-2), 91-95. http://doi.org/10.1016/S0375-9601(96)00729-3

Guo, W., & Xu, X. (2022). Sliding mode control of regulating system of pumped storage power station considering nonlinear pump-turbine characteristics. *Journal of Energy Storage, 52*, 105071. http://doi.org/10.1016/j.est.2022.105071

Hanjra, M. A., & Qureshi, M. E. (2010). Global water crisis and future food security in an era of climate change. *Food Policy, 35*(5), 365-377. http://doi.org/10.1016/j.foodpol.2010.05.006

Jain, S. V., & Patel, R. N. (2014). Investigations on pump running in turbine mode: a review of the state-of-the-art. *Renewable and Sustainable Energy Reviews, 30*, 841-868. http://doi.org/10.1016/j.rser.2013.11.030

Ji, Q., & Zhang, D. (2019). How much does financial development contribute to renewable energy growth and upgrading of energy structure in china? *Energy Policy, 128*, 114-124. http://doi.org/10.1016/j.enpol.2018.12.047

Kan, K., Chen, H., Zheng, Y., Zhou, D., Binama, M., & Dai, J. (2021). Transient characteristics during power-off process in a shaft extension tubular pump by using a suitable numerical model. *Renewable Energy, 164*, 109-121. http://doi.org/10.1016/j.renene.2020.09.001

Kim, H. S., Eykholt, R., & Salas, J. D. (1999). Nonlinear dynamics, delay times, and embedding windows. *Physica. D, 127*(1), 48-60. http://doi.org/10.1016/S0167-2789(98)00240-1

Li, D., Wang, H., Li, Z., Nielsen, T. K., Goyal, R., Wei, X., & Qin, D. (2018). Transient characteristics during the closure of guide vanes in a pump-turbine in pump mode. *Renewable Energy, 118*, 973-983. http://doi.org/10.1016/j.renene.2017.10.088

Liu, M., Tan, L., & Cao, S. (2019). Dynamic mode decomposition of gas-liquid flow in a rotodynamic multiphase pump. *Renewable Energy, 139*, 1159-1175. http://doi.org/10.1016/j.renene.2019.03.015

Matilla-García, M., Morales, I., Rodríguez, J. M., & Ruiz Marín, M. (2021). Selection of embedding dimension and delay time in phase space reconstruction via symbolic dynamics. *Entropy, 23*(2), 221. http://doi.org/10.3390/e23020221

Menter, F. R., Kuntz., M., & Langtry, R. (2003). Ten years of industrial experience with the SST turbulence model. *Turbulence Heat and Mass Transfer, 4*(1), 625-632.

Mezi, I. (2005). Spectral properties of dynamical systems, model reduction and decompositions. *Nonlinear Dynamics, 41*(1-3), 309-325. http://doi.org/10.1007/s11071-005-2824-x

Murakami, T., & Kanemoto, T. (2013). Counter-rotating type pump-turbine unit cooperating with wind power unit. *Journal of Thermal Science, 22*(1), 7-12. http://doi.org/10.1007/s11630-013-0585-2

Nishioka, S. (2023). A challenge for sustainability science: can we halt climate change? *Sustainability Science, 19*, 7-18. http://doi.org/10.1007/s11625-023-01405-1

Rajendra Acharya, U., Paul Joseph, K., Kannathal, N., Lim, C. M., & Suri, J. S. (2006). Heart rate variability: a review. *Medical & Biological Engineering & Computing, 44*(12), 1031-1051. http://doi.org/10.1007/s11517-006-0119-0

Rezaeiha, A., Montazeri, H., & Blocken, B. (2019). On the accuracy of turbulence models for CFD simulations of vertical axis wind turbines. *Energy, 180*, 838-857. http://doi.org/10.1016/j.energy.2019.05.053

Rosenstein, L., Ridgel, A. L., Thota, A., Sarnarne, B., & Alberts, J. L. (2008). Effects of combined robotic therapy and repetitive-task practice on upper-extremity function in a patient with chronic stroke. *American Journal of Occupational Therapy, 62*(1), 28-35. http://doi.org/10.5014/ajot.62.1.28

Sauer, T., Yorke, J., & Casdagli, M. (1991). Embedology. *Journal of Statistical Physics, 65*(3-4), 579-616. http://doi.org/10.1007/BF01053745

Staub, S., Bazan, P., Braimakis, K., Müller, D., Regensburger, C., Scharrer, D., Schmitt, B., Steger, D., German, R., Karellas, S., Pruckner, M., Schlücker, E., Will, S., & Karl, J. (2018). Reversible heat pump–organic rankine cycle systems for the storage of renewable electricity. *Energies, 11*(6), 1352. http://doi.org/10.3390/en11061352

Vick, B. D., & Neal, B. A. (2012). Analysis of off-grid hybrid wind turbine/solar pv water pumping systems. *Solar Energy, 86*(5), 1197-1207. http://doi.org/10.1016/j.solener.2012.01.012

Wanfeng, H., Zhengwei, W., & Honggang, F. (2021). Grid Synchronization of Variable Speed Pump-Turbine Units in Turbine Mode. Renewable Energy, 173, 625-638. http://doi.org/10.1016/j.renene.2021.04.012

Wolf, A., Swift, J., Swinney, H., & Vastano, J. (1985). Determining lyapunov exponents from a time-series. *Physica D-Nonlinear Phenomena, 16*(3), 285-317. https://doi.org/10.1016/0167-2789(85)90011-9

Zhang, F., Zhu, D., Xiao, R., Liu, W., & Tao, R. (2023). Numerical investigation on the transient gas–liquid flow in the rapid switching process of pump turbine. *Energy Science & Engineering*, 1-15. http://doi.org/10.1002/ese3.1482

Zhang, X., Tang, F., Liu, C., Shi, L., Liu, H., Sun, Z., & Hu, W. (2021). Numerical simulation of transient characteristics of start-up transition process of large vertical siphon axial flow pump station. *Frontiers in*

Energy Research, 9, http://doi.org/10.3389/fenrg.2021.706975

Zhao, W., Egusquiza, M., Valero, C., Valentín, D., Presas, A., & Egusquiza, E. (2020). On the use of artificial neural networks for condition monitoring of pump-turbines with extended operation. *Measurement, 163*, 107952. http://doi.org/10.1016/j.measurement.2020.107952

Zheng, Y., Chen, Q., Yan, D., & Liu, W. (2020). A two-stage numerical simulation framework for pumped-storage energy system. *Energy Conversion and Management, 210*, 112676. http://doi.org/10.1016/j.enconman.2020.112676

Zhou, J., Zhang, C., Peng, T., & Xu, Y. (2018). Parameter identification of pump turbine governing system using an improved backtracking search algorithm. *Energies, 11*(7), 1668. http://doi.org/10.3390/en11071668

Zuo, Z., Fan, H., Liu, S., & Wu, Y. (2016). S-shaped characteristics on the performance curves of pump-turbines in turbine mode – A review. *Renewable and Sustainable Energy Reviews, 60*, 836-851. http://doi.org/10.1016/j.rser.2015.12.312